Manipulation of magnetostructural transition and realization of prominent multifunctional magnetoresponsive properties in NiCoMnIn alloys

X. M. Sun,[1] D. Y. Cong,[1,*] Z. Li,[2] Y. L. Zhang,[2] Z. Chen,[1] Y. Ren,[3] K.-D. Liss,[4,5] Z. Y. Ma,[6] R. G. Li,[1] Y. H. Qu,[1] Z. Yang,[1] L. Wang,[7] and Y. D. Wang[1]

[1]*Beijing Advanced Innovation Center for Materials Genome Engineering, State Key Laboratory for Advanced Metals and Materials, University of Science and Technology Beijing, Beijing 100083, China*

[2]*Center for Magnetic Materials and Devices & Key Laboratory for Advanced Functional and Low Dimensional Materials of Yunnan Higher Education Institute, Qujing Normal University, Qujing 655011, China*

[3]*X-ray Science Division, Argonne National Laboratory, Argonne, Illinois 60439, USA*

[4]*Australian Nuclear Science and Technology Organisation, Lucas Heights, New South Wales 2234, Australia*

[5]*Guangdong Technion-Israel Institute of Technology, Shantou 515063, China*

[6]*State Key Laboratory of Heavy Oil Processing, China University of Petroleum, Beijing 102249, China*

[7]*School of Materials Science and Engineering, Beijing Institute of Technology, Beijing 100081, China*

(Received 23 October 2018; published 11 March 2019)

Promising multifunctional magnetoresponsive effects such as magnetoresistance, magnetostrain, and the magnetocaloric effect have recently been extensively studied in Ni-Mn-based metamagnetic shape memory alloys, but large reversible magnetoresponsive effects are usually obtained under high magnetic fields, which is an obstacle for practical applications. Here, through manipulating magnetostructural transition, we achieved large reversible magnetoresponsive effects under a relatively low magnetic field of 3 T in a Ni-Co-Mn-In alloy. By systematically tuning the Mn/In ratio and Co substitution, an optimum composition $Ni_{49}Co_3Mn_{34}In_{14}$ with a low thermal hysteresis (8 K), a narrow transformation interval (7 K) and a high sensitivity of transformation temperature to field change (6 $K\,T^{-1}$), was obtained. Good geometric compatibility between austenite and martensite was revealed by *in situ* synchrotron high-energy x-ray diffraction experiment, which accounts for the low hysteresis and narrow transformation interval. A reversible transformation between pure austenite and pure martensite is induced by a relatively low field of 3 T, which was directly evidenced by *in situ* neutron diffraction experiments. As a result, a large reversible magnetocaloric effect with entropy change of 16.5 $J\,kg^{-1}\,K^{-1}$, a large reversible magnetostrain of 0.26%, and a large reversible magnetoresistance of 60%, under a relatively low field of 3 T, were simultaneously achieved. These reversible magnetoresponsive effects are comparable to the maximum reversible values obtained under high fields in other Ni-Mn-based alloys, but the magnetic field we applied is much lower. This study may guide the design of metamagnetic shape memory alloys with low-field-induced magnetoresponsive properties for magnetic refrigeration, magnetic sensing, and magnetic recording applications.

DOI: 10.1103/PhysRevMaterials.3.034404

I. INTRODUCTION

In recent years, Heusler-type Ni-Mn-based Ni-(Co)-Mn-X (X = Sb, Sn, In) metamagnetic shape memory alloys (MSMAs) undergoing solid-to-solid martensitic transformation have aroused great interest due to their multifunctional magnetoresponsive effects such as magnetoresistance [1–3], magnetostrain [4–6], magnetocaloric effect [7–10], and magnetothermal conductivity [11]. Among these magnetoresponsive effects, magnetoresistance, magnetostrain, and magnetocaloric effect show promising prospects for applications in magnetoresistive heads for magnetic recording devices [12], high-performance actuators [13], and environmentally friendly magnetic refrigerators [14], respectively. The magnetoresponsive effects in Ni-Mn-based MSMAs stem from the magnetic-field-induced first-order magnetostructural transformation from the low-symmetry and weak magnetic martensite to the high-symmetry and ferromagnetic austenite, accompanied with an abrupt change of lattice parameters. The first-order nature of the magnetic-field-induced transformation, on the one hand, leads to much enhanced magnetoresponsive effects, but on the other hand, makes it difficult to transform completely and reversibly between the two phases under low fields owing to the pronounced transformation hysteresis and transformation interval.

Great efforts have been devoted to investigating the magnetoresponsive properties in Ni-Mn-based MSMAs in the past decade. Large magnetoresistance under a magnetic field of 5 T was reported in the $Ni_{41}Co_9Mn_{39}Sb_{11}$ [15], $Ni_{41}Co_9Mn_{40}Sn_{10}$ [16], and $Ni_{50}Mn_{34}In_{16}$ [17] MSMAs, where the magnetoresistance was up to 60, 53.8, and 64%, respectively. Large magnetostrain was obtained under high magnetic fields in a $Ni_{50}Mn_{34}In_{16}$ alloy (0.12% under 5 T) [6] and in a $Ni_{43}Co_7Mn_{39}Sn_{11}$ alloy (0.56% under 8 T) [18], whose

*Corresponding author: dycong@ustb.edu.cn

magnetic work output was considered to be higher than that of the Ni-Mn-Ga alloys [19]. A large magnetocaloric effect under high magnetic fields (above 5 T), with considerable magnetic refrigeration capacity, was reported in various Ni-Mn-based MSMAs [6–8,20,21]. However, almost all of the large and reversible magnetoresponsive properties were obtained under high magnetic fields above 5 T [1–3,5,6,20–27]. If the magnetic field is low, the magnetic-field-induced transformation in Ni-Mn-based MSMAs is largely irreversible due to the coexistence of austenite and martensite across the field-induced transformation, leading to the significant irreversibility of the magnetoresponsive effects which deteriorates the performance during cyclic operation. For practical applications, it is extremely difficult and costly to generate high magnetic fields. Therefore, it is highly desirable to achieve large and reversible magnetoresponsive effects under low magnetic fields. This is the motivation for our present work.

For the sake of realizing complete and reversible transformation and large reversible magnetoresponsive effects under low magnetic fields, it is important to manipulate the magnetostructural transition in MSMAs. In particular, the thermal hysteresis ($\Delta T_{\rm hys}$), phase transformation interval ($\Delta T_{\rm int}$), and sensitivity of transformation temperature to field change are of great relevance [20]. In practice, $\Delta T_{\rm hys}$ and $\Delta T_{\rm int}$ can be estimated as $A_{\rm f}-M_{\rm s}$ and $M_{\rm s}-M_{\rm f}$ ($M_{\rm s}$, $M_{\rm f}$, $A_{\rm s}$, and $A_{\rm f}$ are the martensitic and austenitic transformation start and finish temperatures), respectively [21,27], and the sensitivity of transformation temperature to field change can be estimated with the Clausius-Clapeyron relation [4], which approximately equals $\Delta M/\Delta S_{\rm A}$ (ΔM is the magnetization difference between the two phases and $\Delta S_{\rm A}$ is the transformation entropy change for austenitic transformation). The minimum field required to induce the complete and reversible transformation between austenite and martensite is [21]

$$\Delta(\mu_0 H)_{\rm min} = (\Delta T_{\rm hys} + \Delta T_{\rm int})/(\Delta M/\Delta S_{\rm A}). \quad (1)$$

Apparently, to obtain large reversible magnetoresponsive effects under a low field, the MSMAs should have low $\Delta T_{\rm hys}$, narrow $\Delta T_{\rm int}$, and high $\Delta M/\Delta S_{\rm A}$. It was reported that the value of $\Delta M/\Delta S_{\rm A}$ is closely related to the relative temperature distance between the Curie temperature ($T_{\rm c}$) and austenitic transformation temperature ($T_{\rm A}$, the temperature corresponding to the transformation peak) [28–30]; the larger the $T_{\rm c}-T_{\rm A}$, the larger the $\Delta M/\Delta S_{\rm A}$. Hence, it is viable to tune $\Delta M/\Delta S_{\rm A}$ via tailoring $T_{\rm c}-T_{\rm A}$. In addition, to facilitate practical applications, the large reversible magnetoresponsive effects should occur around room temperature [1,4,31–35]. Since chemical modification has been proved to be an instructive and effective way used to manipulate magnetostructural transition in MSMAs [1,21,26,36–40], in this work we will use this method to synergistically optimize the magnetostructural transition parameters, with the final goal being to achieve large reversible magnetoresponsive effects under low fields.

Among Ni-Mn-based MSMAs, Ni-(Co)-Mn-In alloys have been viewed as very promising candidates for multifunctional magnetoresponsive applications [4,9,14]. The magnetostructural transition in Ni-(Co)-Mn-In alloys can occur within a narrow transformation interval and with a low transformation hysteresis, beneficial for attaining excellent magnetoresponsive properties [1,4,6,9]. Nevertheless, up to now, most studies on the Ni-(Co)-Mn-In system are focused on the Ni-Mn-In alloys with 50 at.% Ni or the Ni-Co-Mn-In alloys in which Co is added to substitute for Ni and the sum of Ni and Co is 50 at.% [1,4,6,9,11,17,22,28,29,41]. Unfortunately, these Ni-(Co)-Mn-In alloys always require high magnetic fields to induce a complete and reversible phase transformation, which severely limits their practical applications. Increasing the Ni content in Ni-(Co)-Mn-In alloys could increase the electron concentration (e/a) and thus raise the martensitic transformation temperature, because in these kinds of alloys the martensitic transformation temperature is strongly correlated with e/a: the higher the e/a, the higher the martensitic transformation temperature [42–44]. This allows substitution of more Co for Ni to form a composition with transformation temperature around room temperature, since substitution of Co for Ni results in decrease of e/a and thus decrease of transformation temperature [34]. Substitution of more Co for Ni could also lead to higher $T_{\rm c}$ and larger $T_{\rm c}-T_{\rm A}$, and thus greater sensitivity of transformation temperature to field change, as mentioned above. Moreover, it was recently reported that the Ni-Mn-In alloys with Ni content higher than 50 at. % possess a relatively small $\Delta T_{\rm hys}+\Delta T_{\rm int}$ [45,46]. Therefore, we envisage that, through manipulating the magnetostructural transition, prominent magnetoresponsive properties could be achieved in the Ni-(Co)-Mn-In alloys with higher Ni content. Here in this work, we selected $Ni_{52}Mn_{35}In_{13}$ as the starting material and systematically tuned the magnetostructural transition parameters via simultaneously tailoring the Mn/In ratio and the amount of Co substitution for Ni. Optimized magnetostructural transition parameters were obtained in the $Ni_{49}Co_3Mn_{34}In_{14}$ alloy. As a result, large reversible near-room-temperature magnetocaloric effect, magnetostrain, and magnetoresistance were successfully achieved under a relatively low magnetic field of 3 T.

II. EXPERIMENT

A total number of 21 polycrystalline button ingots (each of ~40 g) with compositions of $Ni_{52}Mn_{35-x}In_{13+x}$ ($x=0$, 1, 2, 3, and 4), $Ni_{52-y}Co_yMn_{35}In_{13}$ ($y=1$, 2, 3, 4, 5, and 5.2), $Ni_{52-y}Co_yMn_{34}In_{14}$ ($y=1$, 2, 3, 4, and 4.5), $Ni_{52-y}Co_yMn_{33}In_{15}$ ($y=1$, 2 and 3), and $Ni_{52-y}Co_yMn_{32}In_{16}$ ($y=1$ and 2), were prepared by repeated melting (for five times) of the high-purity raw elements (Ni, Co, and In) mixed with the master alloy $Ni_{40}Mn_{60}$ in an arc furnace protected under Ar. Since the master alloy $Ni_{40}Mn_{60}$ was used to alleviate the Mn evaporation during melting, no additional elements were added. The weight loss during repeated melting was less than 0.5 wt. %. For homogeneity, the ingots were sealed into an evacuated quartz tube and then annealed at 1173 K for 24 h followed by quenching into water. The actual composition of the $Ni_{49}Co_3Mn_{34}In_{14}$ alloy was measured with an electron probe microanalyzer (EPMA-1720H, SHIMADZU); the composition was determined by averaging the compositions of five randomly measured points, and it turned out to be $Ni_{48.9\pm0.1}Co_{3.2\pm0.5}Mn_{34.2\pm0.8}In_{13.7\pm0.4}$.

The phase transformation temperatures and transformation entropy change were analyzed by differential scanning calorimetry (DSC) experiments performed with heating and cooling rates of 10 K min^{-1}. The specific heat

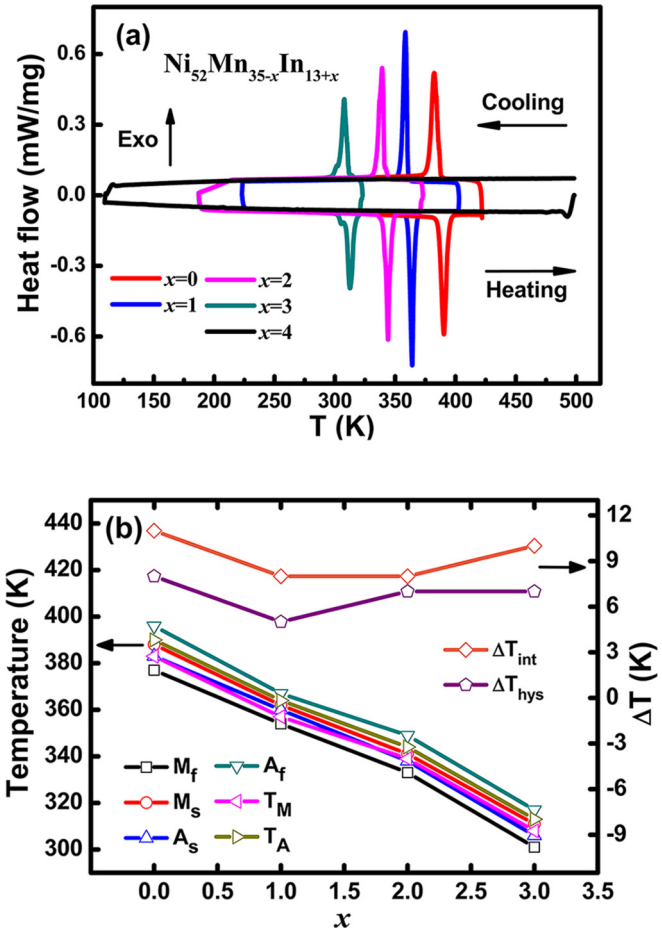

FIG. 1. (a) DSC curves for the $Ni_{52}Mn_{35-x}In_{13+x}$ ($x = 0$, 1, 2, 3, and 4) alloys. (b) Phase transformation temperatures, transformation thermal hysteresis (ΔT_{hys}), and transformation interval (ΔT_{int}) as a function of x.

capacity (C_p) was measured with the modulated DSC technique using a standard sapphire sample with a well-known C_p. The microstructure was characterized by scanning electron microscopy. The magnetic measurements and electrical resistivity measurements were conducted in a physical property measurement system (PPMS, Quantum Design). The magnetostrain was measured by using a strain gauge and a data logger (TDS 150, Tokyo Sokki Kenkyujo Co., Ltd.) under magnetic field up to 3 T provided by PPMS.

The crystal structure evolution during phase transformation was investigated during cooling and heating in the temperature range between 250 K and 290 K by *in situ* synchrotron high-energy x-ray diffraction (HEXRD) experiments carried out at the 11-ID-C beam line of the Advanced Photon Source, Argonne National Laboratory, USA; A monochromatic x-ray beam with a wavelength of 0.1173 Å was used and the diffraction Debye rings were collected by a two-dimensional (2D) large area detector while the sample ($\Phi 2 \times 1\,mm^3$) was rotated at high speed. The crystal structure evolution during magnetic-field-induced transformation was studied during increasing and decreasing magnetic field at 268 and 270 K by *in situ* neutron diffraction experiments, performed on the high intensity diffractometer WOMBAT [47] at the Australian Nuclear Science and Technology Organisation. A wavelength of 2.41 Å was used. The diffracted neutrons were collected on the cylindrical position-sensitive area detector that subtends an angle of 120° on the sample in the diffraction plane and ∼15° in the vertical, out-of-plane direction. For the *in situ* experiments, WOMBAT was equipped with a vertical field magnet (0–11 T) with a temperature range of 1.5–300 K. The disc sample of $\Phi 2 \times 1\,mm^3$ was glued to a pure aluminum bolt for the *in situ* experiments. Considering that the sample possesses a coarse-grained microstructure and there are only a limited number of grains within this sample, reciprocal space mapping was conducted to provide sufficient structural information.

III. RESULTS AND DISCUSSION

A. Magnetostructural transition manipulation

To manipulate the magnetostructural transition for optimal magnetoresponsive properties, we systematically tuned both the Mn/In ratio and the amount of Co substitution for Ni. The DSC curves of $Ni_{52}Mn_{35-x}In_{13+x}$ ($x = 0$, 1, 2, 3, and 4) alloys are plotted in Fig. 1(a). As can be seen, the phase transformation temperatures decrease rapidly with increasing $x(0 \leqslant x \leqslant 3)$. When it comes to $x = 4$, the martensitic transformation cannot be detected within the measured temperature range between 110 and 500 K. For easy visualization, the composition dependence of M_s, T_M, M_f, A_s, T_A, and A_f (T_M is the peak temperature of martensitic transformation) is shown in Fig. 1(b) (see Table I for detailed values). It is worth noting that, for the alloys showing martensitic transformation, even the one ($Ni_{52}Mn_{32}In_{16}$, $x = 3$) with the lowest transformation temperature presents phase transformation above room temperature, which is much higher than the phase transformation temperature (around 220 K) reported for the $Ni_{50}Mn_{34}In_{16}$ alloy [1,6,17,48]. The higher phase transformation temperature of $Ni_{52}Mn_{35-x}In_{13+x}$ ($x = 0$, 1, 2, and 3) offers opportunities for substituting more Co for Ni to attain higher

TABLE I. Martensitic and austenitic transformation characteristic temperatures (K), phase transformation interval ΔT_{int}(K), transformation thermal hysteresis ΔT_{hys}(K), and the entropy change for austenitic (ΔS_A) and martensitic (ΔS_M) transformations ($J\,kg^{-1}\,K^{-1}$) for the $Ni_{52}Mn_{35-x}In_{13+x}$ ($x = 0$, 1, 2, and 3) alloys. The letters "M" and "A" denote martensitic and austenitic transformations, respectively.

x	Alloys	M_s	M_f	A_s	A_f	T_M	T_A	ΔT_{int}	ΔT_{hys}	ΔS_A	ΔS_M
0	$Ni_{52}Mn_{35}In_{13}$	388	377	383	396	383	390	11	8	33.9	33.5
1	$Ni_{52}Mn_{34}In_{14}$	362	354	360	367	357	364	8	5	31.7	30.5
2	$Ni_{52}Mn_{33}In_{15}$	341	333	338	349	339	344	8	7	28.6	28.3
3	$Ni_{52}Mn_{32}In_{16}$	311	301	306	318	308	313	10	7	22.4	21.9

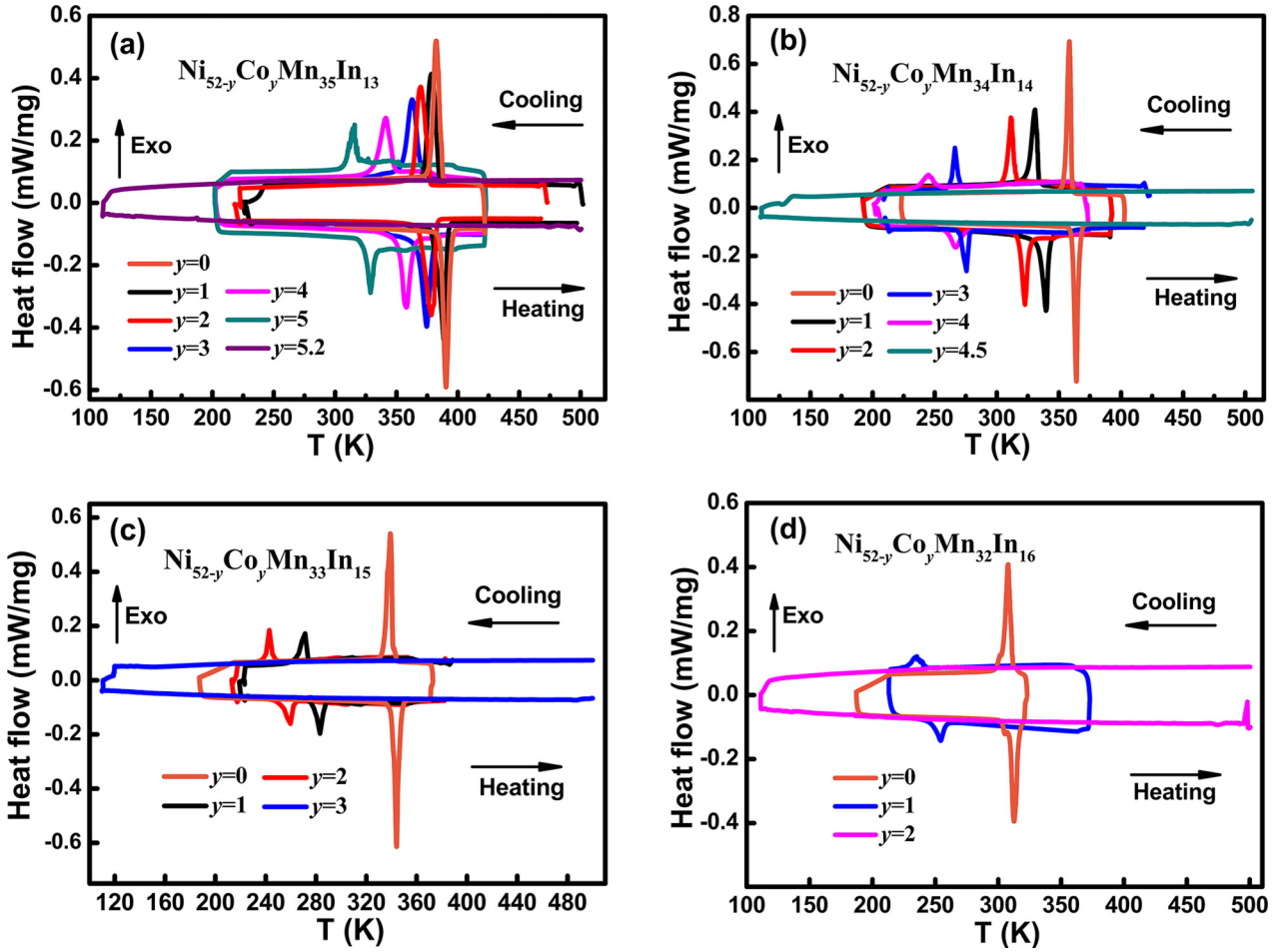

FIG. 2. DSC curves for (a) $Ni_{52-y}Co_yMn_{35}In_{13}$ ($y = 0$, 1, 2, 3, 4, 5, and 5.2), (b) $Ni_{52-y}Co_yMn_{34}In_{14}$ ($y = 0$, 1, 2, 3, 4, and 4.5), (c) $Ni_{52-y}Co_yMn_{33}In_{15}$ ($y = 0$, 1, 2, and 3) and (d) $Ni_{52-y}Co_yMn_{32}In_{16}$ ($y = 0$, 1, and 2) alloys, respectively.

sensitivity of transformation temperature to field change while bringing down the transformation temperature to around room temperature, as mentioned before. The transformation entropy changes for the austenitic transformation (ΔS_A) and martensitic transformation (ΔS_m) estimated from DSC results are also shown in Table I, from which one can see that both ΔS_A and ΔS_m decrease with increasing $x(0 \leqslant x \leqslant 3)$. The influence of transformation entropy change on magnetoresponsive effects will be taken into consideration when manipulating the magnetostructural transition. Figure 1(b) also shows the variation of ΔT_{hys} and ΔT_{int} as a function of x for the $Ni_{52}Mn_{35-x}In_{13+x}$ alloys. Overall, all the $Ni_{52}Mn_{35-x}In_{13+x}$ ($x = 0$, 1, 2, and 3) alloys have relatively small $\Delta T_{hys} + \Delta T_{int}$, beneficial for obtaining a low-field-induced transformation [see Eq. (1)].

Based on the $Ni_{52}Mn_{35-x}In_{13+x}$ ($x = 0$, 1, 2, and 3) alloys, we further substituted Co for Ni to optimize magnetostructural transition parameters. In practice, we increased the amount of Co continuously until no martensitic transformation could be detected in the measurement temperature range between 110 and 500 K. Figures 2(a)–2(d) show the DSC curves of the $Ni_{52-y}Co_yMn_{35}In_{13}$ ($y = 0$, 1, 2, 3, 4, 5, and 5.2), $Ni_{52-y}Co_yMn_{34}In_{14}$ ($y = 0$, 1, 2, 3, 4, and 4.5), $Ni_{52-y}Co_yMn_{33}In_{15}$ ($y = 0$, 1, 2, and 3), and $Ni_{52-y}Co_yMn_{32}In_{16}$ ($y = 0$, 1, and 2) alloys, respectively. For each series of alloys, the phase transformation temperatures decrease with increasing the Co content y, until martensitic transformation disappears in the measurement temperature range at $y = 5.2$ for $Ni_{52-y}Co_yMn_{35}In_{13}$ [Fig. 2(a)], $y = 4.5$ for $Ni_{52-y}Co_yMn_{34}In_{14}$ [Fig. 2(b)], $y = 3$ for $Ni_{52-y}Co_yMn_{33}In_{15}$ [Fig. 2(c)], and $y = 2$ for $Ni_{52-y}Co_yMn_{32}In_{16}$ [Fig. 2(d)]. The detailed phase transformation characteristic parameters of these series of alloys, determined from the DSC curves [Figs. 2(a)–2(d)], are shown in Table II. As can be seen, for each series of alloys, the Curie temperature T_c tends to increase and thus $T_c - T_A$ becomes larger, with increasing y.

As discussed above, to achieve reversible near-room-temperature magnetoresponsive effects under low magnetic field, the alloys should have a small $\Delta T_{hys} + \Delta T_{int}$, a large $T_c - T_A$, and a T_A around room temperature. In addition, an appropriate ΔS_A is essential for achieving a reversible magnetocaloric effect. If ΔS_A is too large, the sensitivity of transformation temperature to field change is low; if ΔS_A is too small, the magnetocaloric effect as a result of magnetic-field-induced transformation is small. Taking into consideration the above criteria, we plotted $\Delta T_{hys} + \Delta T_{int}$ and $T_c - T_A$ together in Fig. 3(a) and ΔS_A and T_A together in Fig. 3(b) for the Co-substituted alloys (shown in Table II), to guide the selection of an optimum composition for

TABLE II. The martensitic and austenitic transformation characteristic temperatures (K), phase transformation interval ΔT_{int} (K), transformation thermal hysteresis ΔT_{hys} (K), $\Delta T_{hys} + \Delta T_{int}$ (K), and the entropy change for austenitic (ΔS_A) and martensitic (ΔS_M) transformations (J kg^{-1} K^{-1}) for the Co-doped Ni-Co-Mn-In alloys. The letters "M" and "A" denote martensitic and austenitic transformations, respectively.

	Alloys	M_s	M_f	A_s	A_f	T_M	T_A	T_c	ΔT_{int}	ΔT_{hys}	$\Delta T_{hys} + \Delta T_{int}$	ΔS_A	ΔS_M
A	$Ni_{51}Co_1Mn_{35}In_{13}$	384	373	379	393	379	388	–	11	9	20	32.8	31.7
B	$Ni_{50}Co_2Mn_{35}In_{13}$	378	364	369	382	370	378	–	14	4	18	30.3	29.4
C	$Ni_{49}Co_3Mn_{35}In_{13}$	370	353	365	379	363	374	380	17	9	26	27.9	27.1
D	$Ni_{48}Co_4Mn_{35}In_{13}$	348	331	350	365	341	358	385	17	17	34	22.1	21.2
E	$Ni_{47}Co_5Mn_{35}In_{13}$	321	308	324	334	315	328	397	13	13	26	19.2	18.4
F	$Ni_{51}Co_1Mn_{34}In_{14}$	335	324	334	344	331	339	345	11	9	20	25.9	25.1
G	$Ni_{50}Co_2Mn_{34}In_{14}$	315	306	317	327	312	322	344	9	12	21	23.7	23
H	$Ni_{49}Co_3Mn_{34}In_{14}$	275	268	276	283	271	279	363	7	8	15	17.6	16.9
I	$Ni_{48}Co_4Mn_{34}In_{14}$	251	238	260	273	245	266	367	13	22	35	13.9	13.1
J	$Ni_{51}Co_1Mn_{33}In_{15}$	274	264	275	288	271	283	354	10	14	24	18.8	17.2
K	$Ni_{50}Co_2Mn_{33}In_{15}$	246	239	250	264	243	259	354	7	18	25	12.3	11.4
L	$Ni_{51}Co_1Mn_{32}In_{16}$	242	229	245	259	235	254	357	13	17	30	11.2	10.5

large and reversible magnetoresponsive effects under low magnetic fields. Clearly, among all the alloys shown in Fig. 3(a), the alloy H ($Ni_{49}Co_3Mn_{34}In_{14}$) shows the smallest $\Delta T_{hys} + \Delta T_{int}$ (15 K) and a relatively large $T_c - T_A$ (84 K). As seen from Fig. 3(b), the alloys H ($Ni_{49}Co_3Mn_{34}In_{14}$) and J ($Ni_{51}Co_1Mn_{33}In_{15}$) both exhibit an appropriate ΔS_A (18.8 J kg^{-1} K^{-1} for $Ni_{51}Co_1Mn_{33}In_{15}$ and 17.6 J kg^{-1} K^{-1} for $Ni_{49}Co_3Mn_{34}In_{14}$) and a near-room-temperature T_A (283 K for $Ni_{51}Co_1Mn_{33}In_{15}$ and 279 K for $Ni_{49}Co_3Mn_{34}In_{14}$). Nevertheless, the alloy J ($Ni_{51}Co_1Mn_{33}In_{15}$) shows a much larger $\Delta T_{hys} + \Delta T_{int}$ and a smaller $T_c - T_A$ as compared with the alloys H ($Ni_{49}Co_3Mn_{34}In_{14}$) [see Fig. 3(a)]. Therefore, we selected $Ni_{49}Co_3Mn_{34}In_{14}$ (H) as the optimum composition. Through magnetostructural transition manipulation, this $Ni_{49}Co_3Mn_{34}In_{14}$ alloy possesses a small $\Delta T_{hys} + \Delta T_{int}$ (15 K), a large $T_c - T_A$ (84 K), a near-room-temperature T_A (279 K), and an appropriate ΔS_A (17.6 J kg^{-1} K^{-1}) and thus we expect that large reversible magnetocaloric effect, magnetostrain, and magnetoresistance could be achieved under a low magnetic field in this alloy. The following investigation will be focused on this alloy.

B. Reversibility of temperature-induced transformation studied by *in situ* synchrotron HEXRD

To trace the structural evolution and the reversibility of phase transformation during cooling and heating in the $Ni_{49}Co_3Mn_{34}In_{14}$ alloy, *in situ* synchrotron HEXRD experiments were carried out. The sample was first cooled from room temperature to 290 and 250 K, and then heated to 290 K. Figures 4(a)–4(c) show the 2D HEXRD patterns collected at 290 K reached by cooling, and 250 and 290 K reached by heating, respectively. By integrating the 2D patterns along the azimuth angle from 0° to 360°, 1D diffraction patterns were obtained and shown in Fig. 4(d). At 290 K, the sample shows an austenitic structure. When cooled to 250 K, the sample transforms into martensite. As can be seen, the 2D HEXRD patterns collected at 290 K reached by cooling [Fig. 4(a)] and 290 K reached by heating [Fig. 4(c)] are almost the same, indicating that the transformation is fully reversible. The 1D diffraction pattern at 250 K [Fig. 4(d)] can all be well indexed according to the six-layered modulated monoclinic martensitic structure (space group No.10, $P2/m$) [21,49] with the lattice parameters of $a_M = 4.4$ Å, $b_M = 5.616$ Å, $c_M = 26.014$ Å, and $\beta = 92.95°$. No residual austenite could be observed at this temperature. This suggests that the transformation is complete. Therefore, during the cooling and heating process, the transformation between austenite and martensite is complete and reversible. Indexation of the 1D diffraction pattern at 290 K [Fig. 4(d)] reveals that the austenite shows a cubic $L2_1$ Heusler structure (space group No. 225, $Fm\bar{3}m$) with the lattice parameter of $a_A = 5.99$ Å.

Utilizing the crystalline symmetry and the lattice parameters of austenite and martensite determined by *in situ* synchrotron HEXRD experiments, we evaluated the geometric compatibility between austenite and martensite, which can be characterized by the middle eigenvalue (λ_2) of the phase transformation stretch matrix **U** [50–56]. It should be noted that HEXRD has high resolution, which ensures the accuracy of the crystal structure information. Our calculation reveals that the λ_2 for the $Ni_{49}Co_3Mn_{34}In_{14}$ alloy is 1.0033, which is fairly close to 1. The comparison of the λ_2 for the present alloy with the values for other Ni-Mn-based MSMAs reported in the literature [9,21,23,36,54] is shown in Fig. 4(e). Usually, good geometric compatibility leads to small thermal hysteresis (ΔT_{hys}) [51]. Besides, recently it was reported that good geometric compatibility also results in narrow transformation temperature interval (ΔT_{int}) and completeness of phase transformation [36,55]. In the present alloy, the excellent geometric compatibility between austenite and martensite accounts for the small $\Delta T_{hys} + \Delta T_{int}$ and the completeness of phase transformation, facilitating a reversible and cyclically stable phase transformation.

To check the reversibility and cyclic stability of phase transformation, which plays a significant role in the functional fatigue of MSMAs, we carried out thermal cycling test across austenitic transformation and martensitic transformation. Figure 5 shows the DSC curves recorded during 100 thermal cycles for the $Ni_{49}Co_3Mn_{34}In_{14}$ alloy. Clearly, no significant shift of the DSC peaks can be observed during 100 thermal

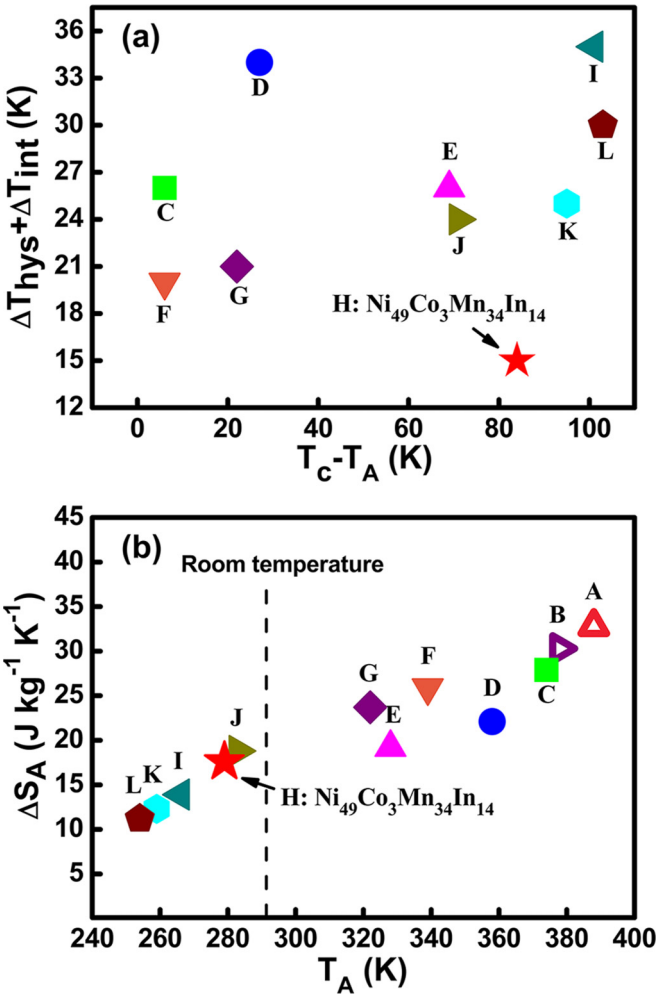

FIG. 3. (a) The sum of phase transformation thermal hysteresis and transformation interval, $\Delta T_{hys} + \Delta T_{int}$, and the relative temperature distance between the Curie temperature and austenitic transformation temperature, $T_c - T_A$, plotted together for the Co-substituted Ni-Mn-In alloys. (b) Austenitic transformation entropy change ΔS_A and austenitic transformation temperature T_A, plotted together for the Co-substituted Ni-Mn-In alloys. The letters "A–L" denote the designed alloys shown in Table II; A: $Ni_{51}Co_1Mn_{35}In_{13}$, B: $Ni_{50}Co_2Mn_{35}In_{13}$, C: $Ni_{49}Co_3Mn_{35}In_{13}$, D: $Ni_{48}Co_4Mn_{35}In_{13}$, E: $Ni_{47}Co_5Mn_{35}In_{13}$, F: $Ni_{51}Co_1Mn_{34}In_{14}$, G: $Ni_{50}Co_2Mn_{34}In_{14}$, H: $Ni_{49}Co_3Mn_{34}In_{14}$, I: $Ni_{48}Co_4Mn_{34}In_{14}$, J: $Ni_{51}Co_1Mn_{33}In_{15}$, K: $Ni_{50}Co_2Mn_{33}In_{15}$, L: $Ni_{51}Co_1Mn_{32}In_{16}$.

cycles. The migration of the martensitic transformation temperatures is within 1 K and the latent heat remains almost unchanged during the cycling test. After the 100 thermal cycles, $\Delta T_{hys} + \Delta T_{int}$ still keeps a small value of 15 K, which is the same as that before thermal cycling. Moreover, the sample remains intact with no cracks observed after 100 thermal cycles (see the inset of Fig. 5). Taken together, these observations indicate good reversibility and cyclic stability of phase transformation in the $Ni_{49}Co_3Mn_{34}In_{14}$ alloy.

C. Magnetic-field-induced complete and reversible transformation evidenced by *in situ* neutron diffraction

As mentioned before, the $Ni_{49}Co_3Mn_{34}In_{14}$ alloy shows a small $\Delta T_{hys} + \Delta T_{int}$ and a large $T_c - T_A$; thus, magnetic-field-induced complete and reversible transformation could be expected under a low magnetic field. Figure 6(a) shows the temperature dependence of magnetization $[M(T)]$ measured under magnetic fields of 0.02 and 3 T for the $Ni_{49}Co_3Mn_{34}In_{14}$ alloy. From the $M(T)$ curve under 0.02 T, M_s, M_f, A_s, A_f, and T_c are determined to be 274, 267, 275, 282, and 363 K, respectively, which are well consistent with the transformation temperatures determined from DSC measurements. As seen from the $M(T)$ curve under 3 T, there is a large magnetization difference (ΔM) of 98 emu g^{-1} between austenite and martensite across the transformation. Comparing the $M(T)$ curves under 0.02 and 3 T, one can see that applying a relatively low magnetic field of 3 T dramatically decreases A_s by about 18 K, with the sensitivity of transformation temperature to field change $\Delta A_s/\Delta(\mu_0 H) \approx 6\,\mathrm{K\,T^{-1}}$. This is in good agreement with the $\Delta M/\Delta S_A$ value (5.6 $\mathrm{K\,T^{-1}}$) estimated based on the results obtained from DSC and $M(T)$ measurements. It is known that if the magnetic-field-induced shift of transformation temperature is larger than $\Delta T_{hys} + \Delta T_{int}$, a reversible magnetic-field-induced transformation can occur in the temperature range between A_s under the magnetic field and M_f under zero field [20,21,27,57]. In order to get insights into the magnetic-field-induced transformation and its reversibility, isothermal magnetization $[M(H)]$ curves were measured during cyclically increasing and decreasing magnetic field in the temperature range from 258 to 270 K with an interval of 2 K and the results are shown in Fig. 6(b). For measurement at each temperature, first the sample was zero-field cooled to 258 K to get a full martensitic state and then heated to the desired temperature for measurement; the field change of 0 T–3 T–0 T was repeated twice for each measurement. As seen from the $M(H)$ curves in Fig. 6(b), this alloy shows a strong metamagnetic transformation behavior between 262 and 270 K, indicating a magnetic-field-induced transformation from weak magnetic martensite to ferromagnetic austenite. At each temperature, the $M(H)$ curves measured during the two cycles of field change almost overlap with each other, suggesting that the magnetic-field-induced transformation is reversible [58]. In the temperature range between 264 and 270 K, the magnetization saturates under the magnetic field of 3 T, implying that the magnetic-field-induced transformation is complete. Therefore, it is inferred that complete and reversible transformation occurs under a relatively low field of 3 T at temperatures between 264 and 270 K. Notably, the magnetic hysteresis (ΔH_{hy}) of the magnetic-field-induced transformation is quite narrow, which is about 1 T. This is the smallest ΔH_{hy} value among those reported for Ni-Mn-based MSMAs [3,4,34,59,60]. Such a narrow ΔH_{hy} will substantially minimize the energy loss during magnetic field cycles [20,35], beneficial for attaining high magnetocaloric performance (especially effective magnetic refrigerant capacity).

To provide direct evidence on the magnetic-field-induced phase transformation as well as its completeness and reversibility, we employed an *in situ* neutron diffraction technique to trace the crystal structure evolution during applying and removing magnetic field. Reciprocal space mapping was carried out during magnetic field change of 0 T–3 T–0 T at 268 and 270 K, respectively. The sample was initially cooled down from room temperature to 250 K to get a full martensitic state and then heated to 268 K for the *in situ* neutron diffraction

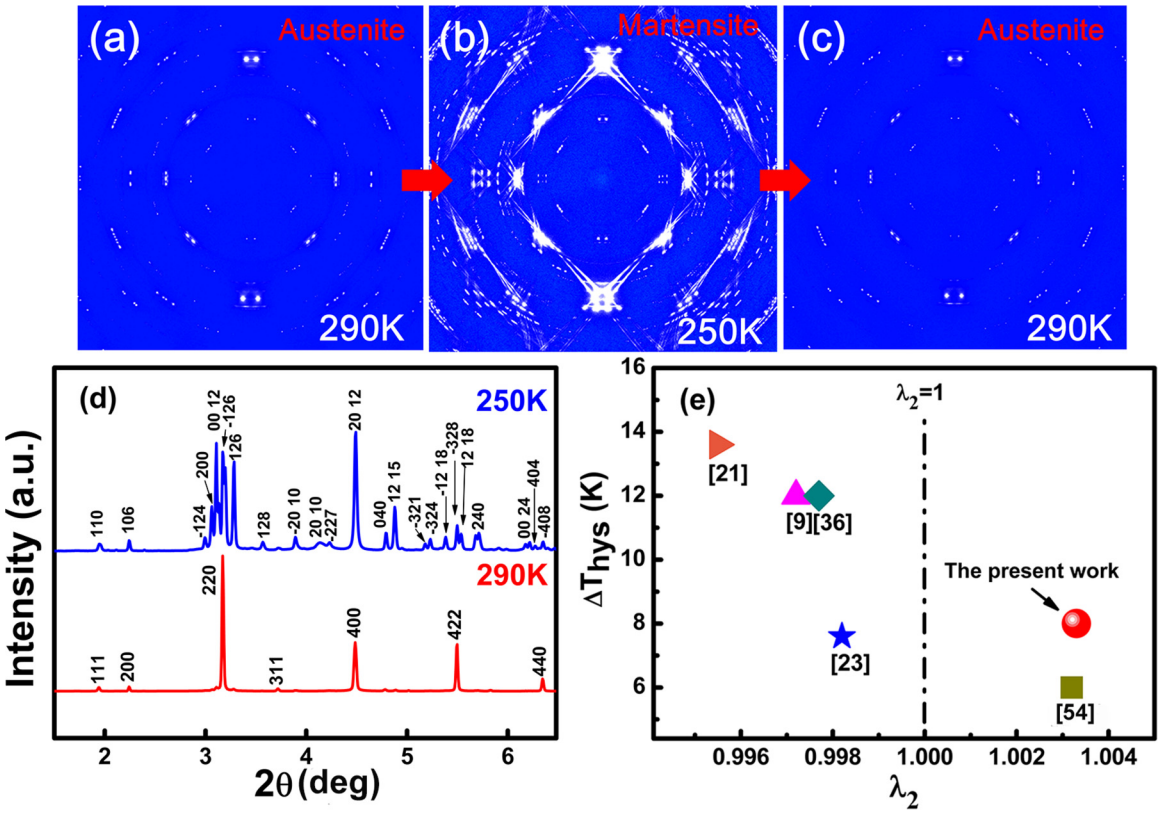

FIG. 4. (a)–(c) Two-dimensional (2D) high-energy x-ray diffraction (HEXRD) patterns experimentally collected at 290 K (reached by cooling) (a), 250 K (reached by cooling) (b), and 290 K (reached by subsequent heating) (c) for $Ni_{49}Co_3Mn_{34}In_{14}$. (d) 1D HEXRD patterns obtained by integrating the 2D patterns in (b) and (c), corresponding to the martensitic and austenitic states, respectively. (e) Correlation between the λ_2 and the thermal hysteresis in typical Ni-Mn-based MSMAs. The compositions corresponding to the reference numbers are [9]–$Ni_{50.4}Mn_{34.8}In_{15.8}$, [21]–$Ni_{41}Ti_1Co_9Mn_{39}Sn_{10}$, [23]–$Ni_{50}Mn_{31.5}In_{16}Cu_{2.5}$, [36]–$Ni_{40}Co_{10}Mn_{40}Sn_9Al_1$, and [54]–$Ni_{45}Co_5Mn_{40}Sn_{10}$.

experiment. The reciprocal space maps measured during increasing and decreasing magnetic field at 268 K are shown in Figs. 7(a)–7(c). The coordinates of the figures are expressed with respect to the scattering vector **Q** with its length $Q = 2\pi/d = 4\pi \sin\theta/\lambda$, with d being the interplanar spacing and 2θ the diffraction angle. To better illustrate the structural evolution during the field change of 0 T–3 T–0 T, in Fig. 7 we only focused on the representative diffraction spots within the Q range from 1.3 to 2.5 $Å^{-1}$, but the other spots out of this range were also taken into consideration when we analyzed the results. Analysis of the diffraction spots in Fig. 7(a) shows that the sample is in a fully martensitic state before applying the magnetic field. When the magnetic field is increased to 3 T, all of the diffraction spots of martensite disappear while the diffraction spot of austenite emerges [Fig. 7(b)], clearly showing the complete magnetic-field-induced transformation from pure martensite to pure austenite. When the magnetic field is decreased from 3 to 0 T, the diffraction spots of martensite reappear and the diffraction spot of austenite completely vanishes [Fig. 7(c)]. The diffraction spots of martensite before applying the magnetic field [Fig. 7(a)] and after removing the magnetic field [Fig. 7(c)] are almost identical, demonstrating that the magnetic-field-induced transformation is fully reversible. Overall, Figs. 7(a)–7(c) unambiguously confirm that the sample can transform completely and reversibly between austenite and martensite under a relatively low magnetic field of 3 T at 268 K. This corresponds well to the $M(H)$ curve at 268 K shown in Fig. 6(b). After the *in situ* neutron diffraction experiment at 268 K, the sample is heated to 270 K where all of the diffraction spots still indicate a fully martensitic

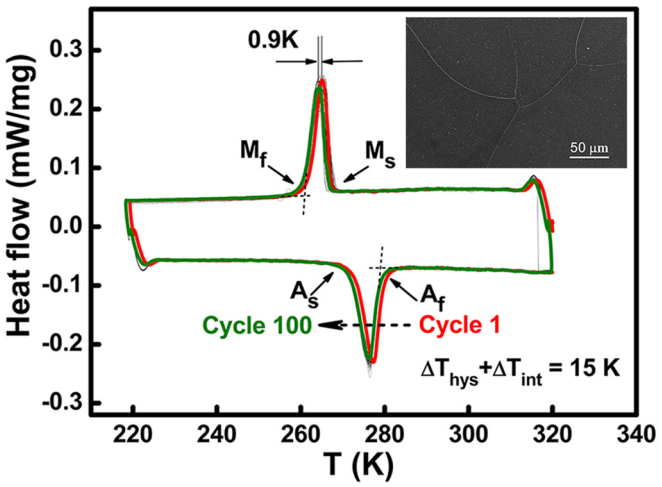

FIG. 5. DSC curves recorded during 100 thermal cycles across martensitic transformation and austenitic transformation for $Ni_{49}Co_3Mn_{34}In_{14}$. The inset shows the microstructure of the sample after 100 thermal cycles.

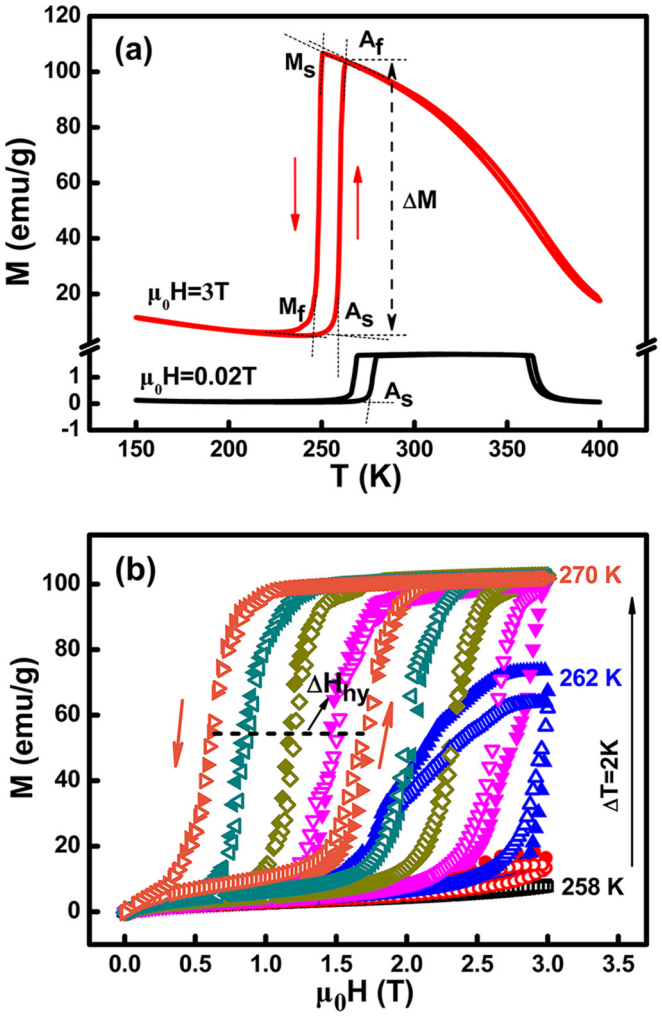

FIG. 6. (a) Temperature dependence of magnetization [$M(T)$] measured under magnetic fields of 0.02 T and 3 T, respectively, for $Ni_{49}Co_3Mn_{34}In_{14}$. (b) Two cycles of isothermal magnetization [$M(H)$] curves recorded at constant temperatures from 258 to 270 K with an interval of 2 K for $Ni_{49}Co_3Mn_{34}In_{14}$.

structure [Fig. 7(d)]. Upon applying a magnetic field of 3 T at 270 K, the martensite transforms completely into austenite [Fig. 7(e)]. After removing the magnetic field, the field-induced austenite mostly transforms back to martensite [Fig. 7(f)], but there is still a tiny amount of residual austenite as suggested by the weak intensity of the $(200)_A$ diffraction spot in Fig. 7(f).

For a more comprehensive analysis, the evolution of the 1D diffraction patterns, obtained by azimuthal integration of the reciprocal space maps, during applying and removing magnetic field at 268 and 270 K, are shown in Figs. 7(g) and 7(h), respectively. Based on the 1D diffraction patterns, the completeness and reversibility of magnetic-field-induced transformation under 3 T at 268 and 270 K are clearly presented. The above *in situ* neutron diffraction experiment clearly evidences that a complete and reversible magnetic-field-induced transformation occurs under a relatively low magnetic field of 3 T in the $Ni_{49}Co_3Mn_{34}In_{14}$ alloy. Thus, large reversible multifunctional magnetoresponsive effects can be expected under a relatively low field of 3 T in this alloy.

D. Magnetocaloric effect

To examine the magnetocaloric effect under a magnetic field of 3 T, we first evaluated the magnetic entropy change (ΔS_m) which is one important characteristic parameter for the magnetocaloric effect [9,20,35]. Based on the $M(H)$ curves shown in Fig. 6(b) [for clarity, the $M(H)$ curves recorded during increasing magnetic field in the second cycle are displayed in the inset of Fig. 8], ΔS_m is estimated using the Maxwell relation:

$$\Delta S_m = S_m(T, H) - S_m(T, 0) = \int_0^{\mu_0 H} \frac{\partial M}{\partial T} d(\mu_0, H). \quad (2)$$

It should be noted that ΔS_m is usually overestimated with the Maxwell relation if there is a phase coexistence of the weak magnetic martensite and ferromagnetic austenite before applying a magnetic field [61,62]. Fortunately, our $Ni_{49}Co_3Mn_{34}In_{14}$ alloy is in the pure martensitic state before applying a magnetic field at each temperature at which the $M(H)$ curves in Fig. 6(b) were recorded; in this case, the ΔS_m estimated with the Maxwell relation is reliable [20,62]. The estimated ΔS_m under 3 T is shown as a function of temperature in Fig. 8. Clearly, the maximum value of ΔS_m under 3 T is $\sim$16.5 J kg^{-1} K^{-1}, which is very close to the transformation entropy change ΔS_A (17.6 J kg^{-1} K^{-1}) determined from the DSC curve in Fig. 2(b) (see Table II). Since the magnetic-field-induced transformation is reversible (as demonstrated above in Sec. III C), the ΔS_m as a result of such transformation is also reversible. Therefore, a large reversible ΔS_m of 16.5 J kg^{-1} K^{-1} is achieved under a relatively low field of 3 T in the $Ni_{49}Co_3Mn_{34}In_{14}$ alloy. Table III lists the reversible ΔS_m obtained in Ni-Mn-based MSMAs [20,21,27,63,64]. As can be seen, the magnitude of the reversible ΔS_m we achieved is comparable to that obtained under higher fields (above 5 T) in other Ni-Mn-based alloys [20,21,27,63,64], but the magnetic field we applied is significantly lower, which is indeed beneficial for practical applications.

The adiabatic temperature change ΔT_{ad} is another important characteristic parameter for magnetocaloric effect. It was reported that the reversible ΔT_{ad} can be estimated on the basis of the reversible ΔS_m data by using the following relation [9]:

$$\Delta T_{ad} = -\frac{T}{C_p} \cdot \Delta S_m, \quad (3)$$

where C_p is the specific heat capacity obtained at the temperature T. The C_p in the $Ni_{49}Co_3Mn_{34}In_{14}$ alloy is determined by using the modulated DSC technique and it is shown as a function of temperature in Fig. 9(a). Using the reversible ΔS_m data shown in Fig. 8 and the C_p values presented in Fig. 9(a), the reversible ΔT_{ad} is computed with Eq. (3) and shown as a function of temperature in Fig. 9(b). As can be seen, the maximum reversible ΔT_{ad} under 3 T is about -9.7 K, which actually is a large reversible ΔT_{ad} under such a relatively low field.

For magnetic refrigeration, the refrigerant capacity (*RC*) is often used to evaluate the potential magnetic cooling efficiency of the magnetocaloric materials for practical

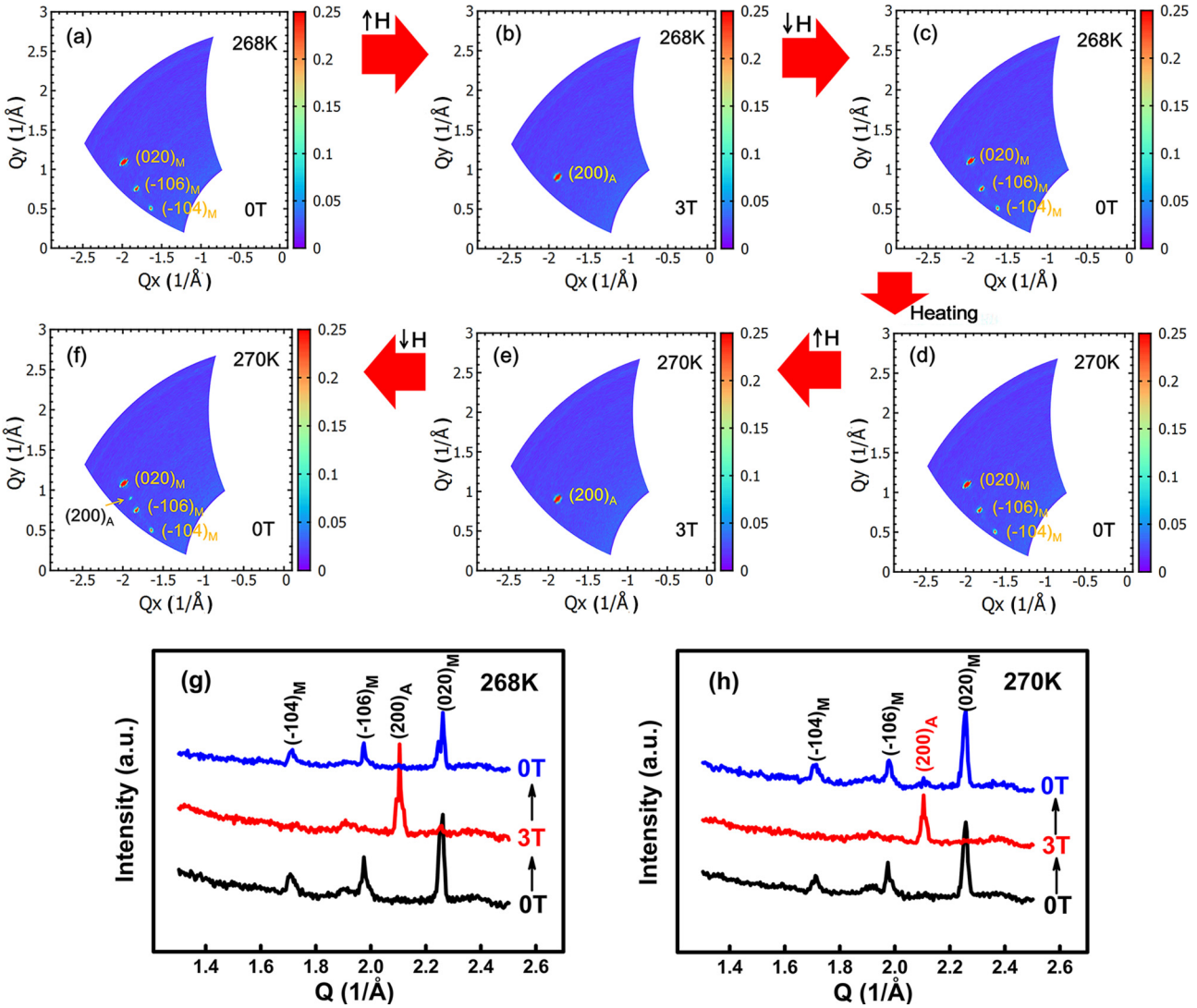

FIG. 7. (a)–(c) Reciprocal space maps measured at 268 K during increasing magnetic field from 0 T (a) to 3 T (b) and then decreasing magnetic field to 0 T (c) for $Ni_{49}Co_3Mn_{34}In_{14}$. (d)–(f) Reciprocal space maps measured at 270 K during increasing magnetic field from 0 T (d) to 3 T (e) and then decreasing magnetic field to 0 T (f) for $Ni_{49}Co_3Mn_{34}In_{14}$. (g), (h) 1D diffraction patterns obtained by azimuthal integration of the reciprocal space maps shown in (a)–(c) measured at 268 K (g) and (d)–(f) measured at 270 K (h), respectively. The letters "A" and "M" in the indices denote austenite and martensite, respectively. The coordinates of the figures are expressed with respect to the scattering vector **Q** with its length $Q = 2\pi/d = 4\pi \sin\theta/\lambda$, with d being the interplanar spacing and 2θ the diffraction angle.

applications [34,35]. The *RC* for a reversible refrigeration cycle is defined as [35,65]:

$$RC = \int_{T_{cold}}^{T_{hot}} \Delta S_m dT \tag{4}$$

where T_{cold} (the temperature of the cold reservoir) and T_{hot} (the temperature of the hot reservoir) correspond to the temperatures at full width half maximum of the ΔS_m peak [65]. Using Eq. (4), the *RC* under 3 T is estimated to be $\sim 116.6\,J\,kg^{-1}$. It should be noted that, for magnetocaloric materials with negligible hysteresis loss, Eq. (4) can be used to reasonably evaluate the magnetic cooling efficiency [20,65–67], but for the materials with apparent magnetic hysteresis (e.g., Ni-Mn-based MSMAs), it is more reliable to use the effective refrigerant capacity RC_{eff}, computed by taking the average hysteresis loss away from the *RC* value, to evaluate the final cooling efficiency for cyclic applications [68]. In the $Ni_{49}Co_3Mn_{34}In_{14}$ alloy, a narrow ΔH_{hy} of ~ 1 T [Fig. 6(b)] leads to a relatively small hysteresis loss of $\sim 42.1\,J\,kg^{-1}$. Consequently, a RC_{eff} value of $\sim 74.5\,J\,kg^{-1}$ is obtained under 3 T in the present alloy. Considering that the magnetic-field-induced transformation is reversible and repeatable (as inferred from Fig. 6), the magnetic hysteresis loss and thus the RC_{eff} is consistent during magnetic cycling. Actually, this large repeatable RC_{eff} ($\sim 74.5\,J\,kg^{-1}$) under 3 T is comparable to that obtained under a high magnetic field of 5 T ($\sim 76.6\,J\,kg^{-1}$) in other Ni-Mn-based alloys [20]. As demonstrated above, a large reversible magnetocaloric effect, with ΔS_m of $16.5\,J\,kg^{-1}\,K^{-1}$ and RC_{eff} of $\sim 74.5\,J\,kg^{-1}$, is achieved under a relatively low field of 3 T in the $Ni_{49}Co_3Mn_{34}In_{14}$ alloy.

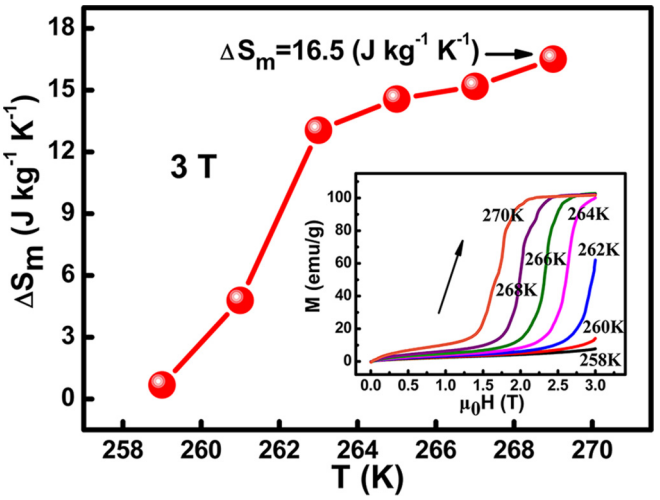

FIG. 8. Reversible magnetic entropy change (ΔS_M) under a magnetic field of 3 T shown as a function of temperature. The inset shows the $M(H)$ curves extracted from Fig. 6(b); for clarity, only the curves recorded during increasing magnetic field in the second cycle are displayed.

E. Magnetostrain

The magnetic-field-induced transformation in Ni-Co-Mn-In alloys usually results in a magnetostrain effect [4]. We investigated the magnetostrain under a magnetic field of 3 T in the $Ni_{49}Co_3Mn_{34}In_{14}$ alloy by measuring the strain during increasing and decreasing magnetic field. A cubic sample with the size of $7 \times 7 \times 7\,mm^3$ was used for the magnetostrain measurements. It was cut from the button ingot, with four edges parallel to the solidification direction of the ingot, as illustrated in Fig. 10(a). Owing to the temperature gradient along the solidification direction when the ingot was prepared in a water-cooled copper crucible, preferred crystallographic orientation forms in the ingot. The annealed ingot consists of columnar grains showing a texture with ⟨001⟩ of austenite parallel to the solidification direction [25,26,68]. For the magnetostrain measurements, the magnetic field is always applied along the solidification direction, while the strain is measured in the directions both parallel and perpendicular to the solidification direction (Fig. 10). The magnetostrain is defined as

$$\Delta L/L_0 = [L(H) - L_0]/L_0, \tag{5}$$

where L_0 is the length under zero field and $L(H)$ is the length under a magnetic field $\mu_0 H$. Before the measurement at each temperature, the sample was first cooled down to 256 K under zero field to ensure a full martensitic state and then heated to the measurement temperature.

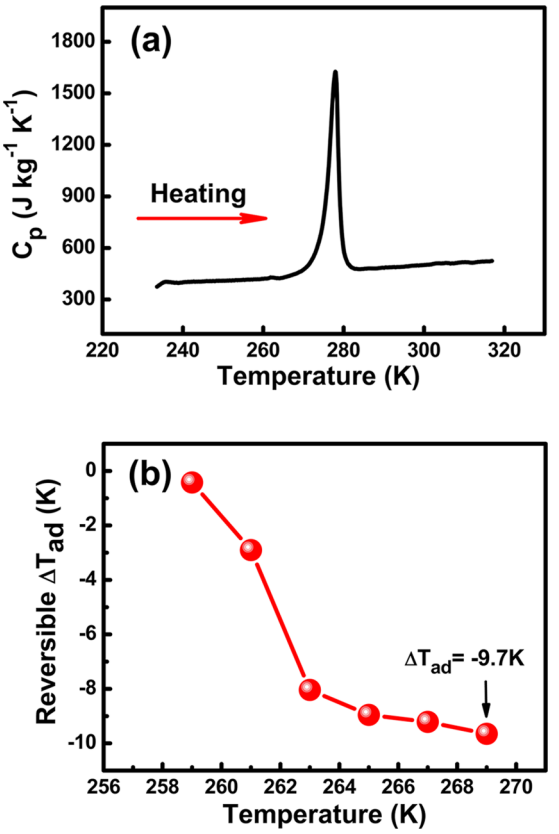

FIG. 9. (a) Specific heat capacity C_p measured by using the modulated DSC technique shown as a function of temperature for $Ni_{49}Co_3Mn_{34}In_{14}$. The result is for the heating process. (b) Reversible adiabatic temperature change ΔT_{ad} under a magnetic field of 3 T, estimated with Eq. (3), shown as a function of temperature.

Figure 10(b) shows the magnetostrain parallel to the solidification direction measured at 260, 264, and 268 K in the polycrystalline $Ni_{49}Co_3Mn_{34}In_{14}$ alloy. One can see that at each temperature the strain shows an obvious increase above a critical magnetic field, which is owing to the magnetic-field-induced transformation, and recovers fully to the initial state after removing the field. The magnetostrain under 3 T is about 0.025% at 260 K, and it increases to about 0.07% at 264 K. This is because of the increased fraction of magnetic-field-induced transformation. The magnetostrain under 3 T

TABLE III. Magnetic-field-induced reversible ΔS_m in the $Ni_{49}Co_3Mn_{34}In_{14}$ alloy (this work) compared with that reported in other Ni-Mn-based alloys. "T" denotes the temperature at which the reversible ΔS_m is obtained.

Alloys	ΔS_m (J kg^{-1} K^{-1})	T (K)	Applied field (T)	References
$Ni_{49}Co_3Mn_{34}In_{14}$	16.5	269	3	This work
$Ni_{49.8}Co_{1.2}Mn_{33.5}In_{15.5}$	14.6	236	5	[20]
$Ni_{41}Ti_1Co_9Mn_{39}Sn_{10}$	18.7	285	5	[21]
$Ni_{48.1}Co_{2.9}Mn_{35.0}In_{14.0}$	12.8	233	5	[27]
$Ni_{42.47}Co_{8.87}Mn_{31.67}Ga_{14.98}In_{2.01}$	8	413	6	[63]
$Ni_{43}Co_6Mn_{40}Sn_{11}$	19.3	266	5	[64]

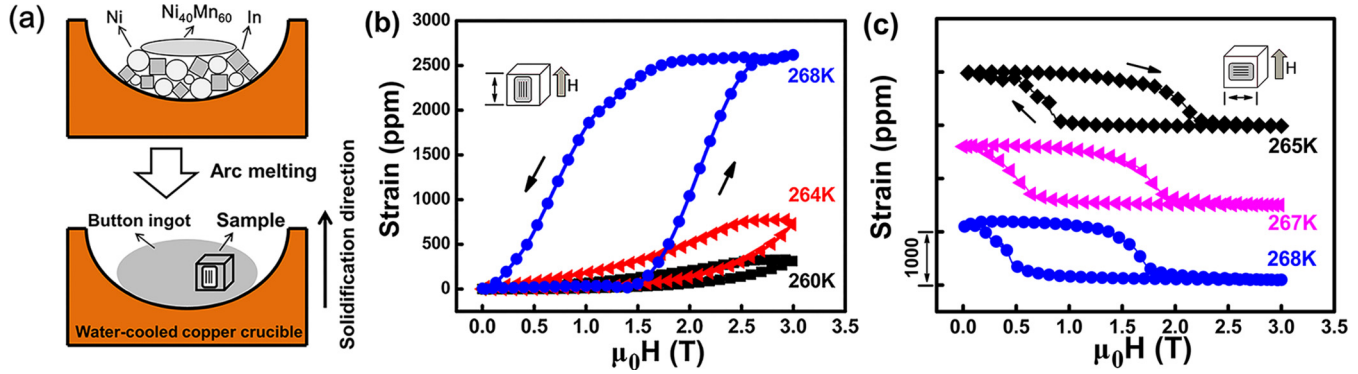

FIG. 10. (a) Illustration of how the cubic sample ($7 \times 7 \times 7\,\mathrm{mm}^3$) for magnetostrain measurements was cut from the button ingot. (b) Magnetostrain parallel to the solidification direction measured at 260, 264, and 268 K in the polycrystalline $Ni_{49}Co_3Mn_{34}In_{14}$ alloy. (c) Magnetostrain perpendicular to the solidification direction measured at 265, 267, and 268 K in the polycrystalline $Ni_{49}Co_3Mn_{34}In_{14}$ alloy.

reaches 0.26% at 268 K, at which the complete transformation is induced. Therefore, a large reversible magnetostrain up to 0.26% is achieved under a relatively low magnetic field of 3 T in the polycrystalline $Ni_{49}Co_3Mn_{34}In_{14}$ alloy. The magnetostrain perpendicular to the solidification direction in the same sample is also measured and the results are shown in Fig. 10(c). At all the measurement temperatures (265, 267, and 268 K), the magnetic-field-induced transformation is reversible and complete at 3 T, and hence the magnetostrain at 3 T (which is fully reversible) is approximately the same at these temperatures, i.e., −0.12%. Apparently, the magnetostrain perpendicular to the solidification direction shows a negative sign and has a magnitude much smaller than that parallel to the solidification direction [Fig. 10(b)]. This is attributed to the anisotropy of microstructure and crystallographic orientation in the button ingot solidified in a water-cooled copper crucible [25,26,68–70].

To evaluate the repeatability of magnetostrain during different magnetic cycles, we continued to examine the magnetostrain during cyclic application and removal of magnetic field after the measurement shown in Fig. 10(c). The magnetostrain perpendicular to the solidification direction measured during two field cycles at different temperatures is displayed in Fig. 11. At 267 K [Fig. 11(a)] and 268 K [Fig. 11(b)], the magnetostrain exhibits almost the same field dependence during the first and second cycles of increasing and decreasing magnetic field. Further measurements at 268 K shows that the magnetostrain *vs* field curves recorded during the third and fourth cycles (for clarity, not shown here) coincide well with those recorded during the first and second field cycles. This clearly demonstrates the excellent repeatability of the magnetostrain in the $Ni_{49}Co_3Mn_{34}In_{14}$ alloy. As seen from Figs. 11(c) and 11(d), when the measurement temperature increases to 270 and 271 K, the magnetostrain during the first field cycle could not fully recover after removing the field, which is attributed to the residual field-induced austenite as revealed by our *in situ* neutron diffraction experiment [Fig. 7(f)]. Fortunately, the magnetostrain (–0.1% at 3 T) becomes fully reversible and repeatable from the second cycle [Figs. 11(c) and 11(d)].

As demonstrated above, a large reversible magnetostrain of up to 0.26% is achieved under a relatively low field of 3 T in the polycrystalline $Ni_{49}Co_3Mn_{34}In_{14}$ alloy. Table IV lists the reversible magnetostrain obtained in Ni-Mn-based MSMAs [5,6,24,26,71]. Since only the reversible magnetostrain is useful for cyclic actuation, the irreversible magnetostrain reported in the literature is not included in this table. As can be seen, the large reversible magnetostrain can only be obtained with a high magnetic field above 5 T in the literature. In contrast, we only applied a relatively low magnetic field of 3 T to attain a large reversible strain of 0.26%, thanks to the optimized magnetostructural transition parameters in the studied alloy. The reduction of the actuation magnetic field is important for practical applications. It is worth mentioning that predeformation or thermal-mechanical training [4,5,24] is not needed to get the large reversible magnetostrain in the present work. In addition, the large reversible magnetostrain is achieved in the polycrystals, which are easier to synthesize as compared with single crystals, which, from the technological point of view, facilitates the applications of this material.

F. Magnetoresistance

Owing to the difference in the resistivity of austenite and martensite in Ni-Mn-based MSMAs, there is a change in resistivity during the magnetic-field-induced transformation, giving rise to a magnetoresistance effect. To examine the magnetoresistance under a magnetic field of 3 T, we studied the variation of electrical resistance with temperature and magnetic field in the $Ni_{49}Co_3Mn_{34}In_{14}$ alloy. Figure 12(a) illustrates the temperature dependence of the electrical resistance [$\rho(T)$] measured under 0 T and 3 T. As seen from the $\rho(T)$ curves, during cooling the electrical resistance undergoes an abrupt increase upon martensitic transformation. This is related with the variation of the density of electronic states in the vicinity of the Fermi surface during phase transformation [1,17,72]. Remarkably, the electrical resistance of martensite is three times as large as that of austenite. Comparing the $\rho(T)$ curves under 0 and 3 T [Fig. 12(a)], one can see that the transformation temperature A_s is significantly decreased by 17 K under a field of 3 T, with $\Delta A_s/\Delta(\mu_0 H) \approx 5.7\,\mathrm{K\,T^{-1}}$, which is well consistent with the result obtained from the $M(T)$ curves [Fig. 6(a)]. If a magnetic field of 3 T is applied at a temperature close to A_s (under 0 T), there will be a magnetic-field-induced transformation from martensite to

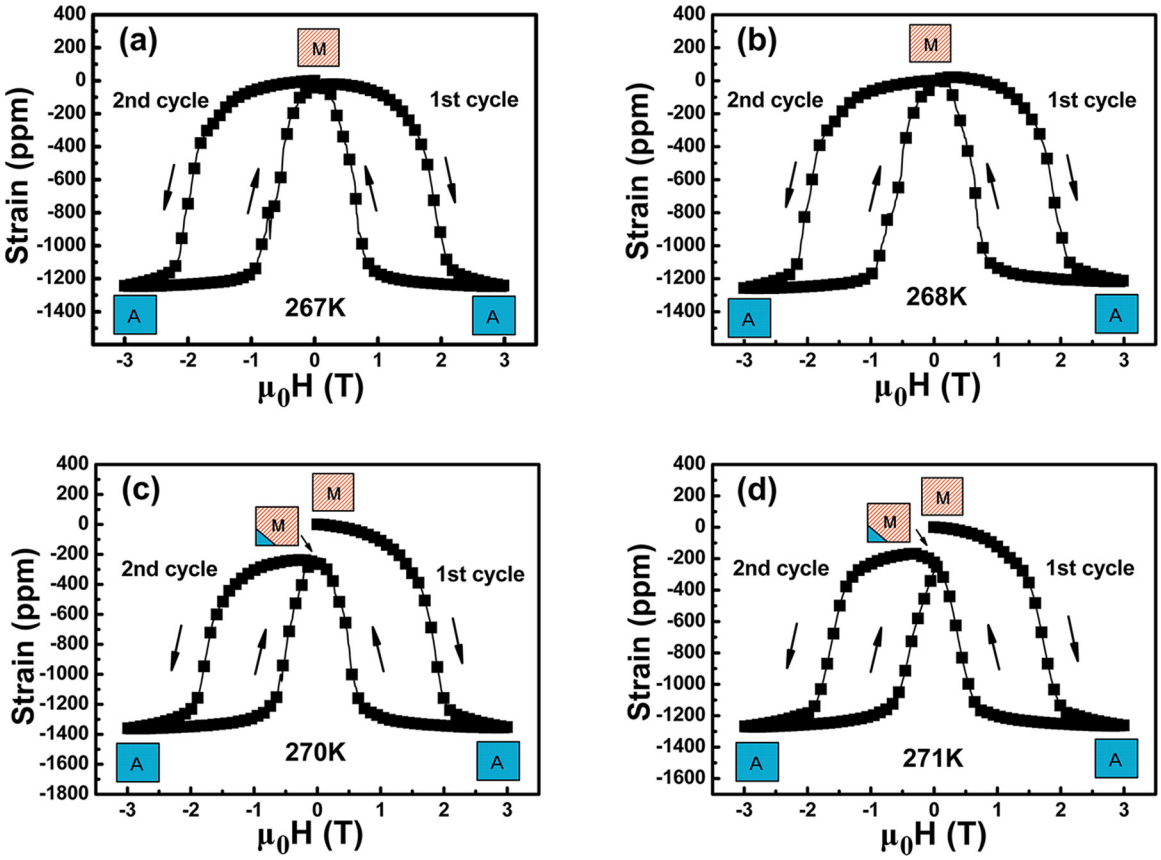

FIG. 11. Magnetostrain perpendicular to the solidification direction measured during two field cycles at (a) 267 K, (b) 268 K, (c) 270 K, and (d) 271 K in the polycrystalline $Ni_{49}Co_3Mn_{34}In_{14}$ alloy.

austenite leading to a significant decrease of electrical resistance, and thus a large magnetoresistance can be expected.

The electrical resistance during increasing and decreasing magnetic field was measured and the magnetoresistance under a magnetic field $\mu_0 H$ was obtained from the following relation:

$$\Delta R/R_0 = (R_H - R_0)/R_0, \quad (6)$$

where R_0 is the electrical resistance under zero field and R_H is the electrical resistance under $\mu_0 H$. Figure 12(b) displays the magnetoresistance as a function of magnetic field [$\rho(H)$] at 240, 260, 264, and 268 K for $Ni_{49}Co_3Mn_{34}In_{14}$, where the sample is in the fully martensitic state before applying magnetic field at each temperature. As can be seen, the magnetoresistance abruptly increases above a critical magnetic field at 260, 264, and 268 K, which is attributed to the magnetic-field-induced transformation from martensite to austenite; the magnetoresistance recovers to zero after removing the field, indicating that the magnetoresistance in the present alloy is fully reversible. The magnetoresistance shows a negative value owing to the lower electrical resistance of austenite, and it amounts to 19 and 38% (under 3 T) at 260 and 264 K, respectively. Notably, the magnetoresistance under 3 T reaches a high value of 60% at 268 K. Thus, a large reversible magnetoresistance is achieved under a relatively low magnetic field of 3 T in the $Ni_{49}Co_3Mn_{34}In_{14}$ alloy. For comparison, Table V lists the reversible magnetoresistance obtained in Ni-Mn-based MSMAs [1,3,73–75]. As can be seen, the large

TABLE IV. Magnetic-field-induced reversible magnetostrain in the $Ni_{49}Co_3Mn_{34}In_{14}$ alloy (this work) compared with that reported in other Ni-Mn-based alloys. "T" denotes the temperature at which the reversible magnetostrain is obtained. The letters "S" in the bracket denotes single crystal; the other alloys are all polycrystalline.

Ni-Mn-based alloys	Magnetostrain (%)	T (K)	Applied field (T)	References
$Ni_{49}Co_3Mn_{34}In_{14}$	0.26	268	3	This work
$Ni_{43}Co_7Mn_{39}Sn_{11}$	0.3	310	8	[5]
$Ni_{50}Mn_{34}In_{16}$	0.12	195	5	[6]
$Ni_{30}Cu_8Co_{12}Mn_{37}Ga_{13}$(S)	0.47	264	9	[24]
$Ni_{50}Mn_{33}In_{13}Ga_4$	0.49	194	7	[26]
$Ni_{46}Co_4Mn_{39}Sn_{11}$	0.012	225	3	[71]

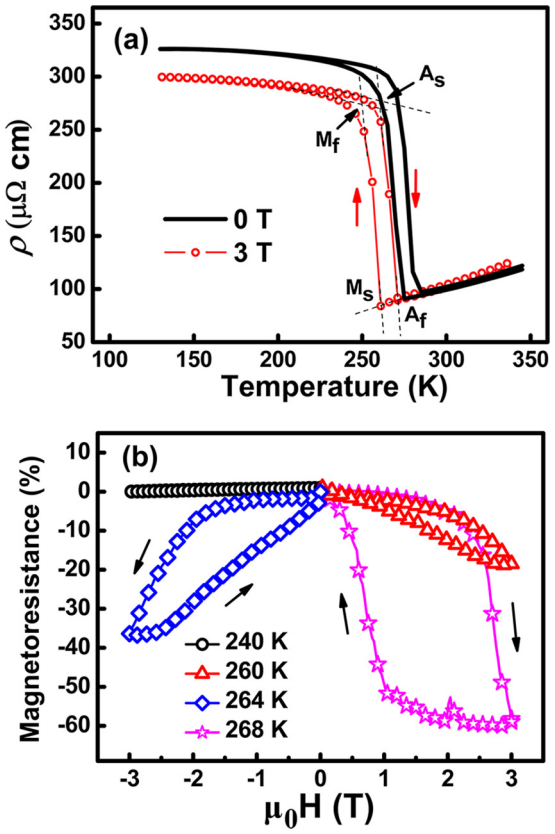

FIG. 12. (a) Temperature dependence of electrical resistance [$\rho(T)$] measured under 0 and 3 T, respectively, for $Ni_{49}Co_3Mn_{34}In_{14}$. (b) Variation of magnetoresistance as a function of magnetic field [$\rho(H)$] measured at 240, 260, 264, and 268 K, respectively, for $Ni_{49}Co_3Mn_{34}In_{14}$.

reversible magnetoresistance we achieved under a relatively low field of 3 T is comparable to that obtained under higher fields (e.g., 9 T) in other Ni-Mn-based alloys. Moreover, the large reversible magnetoresistance in the present work is achieved around room temperature whereas that reported in the literature is usually obtained at temperatures much lower than room temperature (below 240 K, see Table V). The lower actuation magnetic field and the near-room-temperature working temperature benefit the applications of the magnetoresistance in the present $Ni_{49}Co_3Mn_{34}In_{14}$ alloy.

IV. CONCLUSIONS

The magnetostructural transition in the Ni-(Co)-Mn-In MSMAs was manipulated via systematically tuning the Mn/In ratio and the Co substitution in a series of compositions. An optimum composition $Ni_{49}Co_3Mn_{34}In_{14}$ with best combination of magnetostructural transition parameters was singled out. This $Ni_{49}Co_3Mn_{34}In_{14}$ alloy shows a small $\Delta T_{hys} + \Delta T_{int}$ of 15 K and a high sensitivity of transformation temperature to field change, 6 $K\,T^{-1}$. A reversible magnetic-field-induced transformation between pure martensite and pure austenite occurs under a relatively low magnetic field of 3 T in this alloy, which is directly evidenced by our *in situ* neutron diffraction experiment. Based on this magnetic-field-induced transformation, large reversible multifunctional magnetoresponsive effects were obtained. A large reversible magnetocaloric effect with ΔS_m of 16.5 $J\,kg^{-1}\,K^{-1}$, a large reversible magnetostrain of 0.26% and a large reversible magnetoresistance of 60%, under a relatively low magnetic field of 3 T, were simultaneously achieved in this $Ni_{49}Co_3Mn_{34}In_{14}$ alloy. The magnitudes of these reversible magnetoresponsive effects are comparable to those reported under high magnetic fields (above 5 T) in other Ni-Mn-based MSMAs, but the magnetic field required to induce the magnetoresponsive effects in the present work is drastically lower. Moreover, the large reversible magnetoresponsive effects in $Ni_{49}Co_3Mn_{34}In_{14}$ were obtained around room temperature. The reduced actuation magnetic field and the near-room-temperature working temperature of $Ni_{49}Co_3Mn_{34}In_{14}$ are quite beneficial for the practical applications of the magnetoresponsive effects. The present work may guide the design of high-performance MSMAs with extraordinary low-field-induced multifunctional magnetoresponsive properties.

ACKNOWLEDGMENTS

We thank Dr. D. E. Brown for useful discussions. G. Davidson and R. Spence are gratefully acknowledged for their technical support on the sample environment. This work is supported by the National Natural Science Foundation of China (Grants No. 51731005, No. 51822102, and No. 51831003). Use of the Advanced Photon Source was supported by the U.S. Department of Energy, Office of Science, Office of Basic Energy Science, under Contract No. DE-AC02-06CH11357.

TABLE V. Magnetic-field-induced reversible magnetoresistance in the $Ni_{49}Co_3Mn_{34}In_{14}$ alloy (this work) compared with that reported in other Ni-Mn-based alloys. "T" denotes the temperature at which the reversible magnetoresistance is obtained.

Ni-Mn-based alloys	Magnetoresistance (%)	T (K)	Applied field (T)	References
$Ni_{49}Co_3Mn_{34}In_{14}$	60	268	3	This work
$Ni_{50}Mn_{35}In_{15}$	80	150	9	[1]
$Ni_{41}Co_9Mn_{39}Sb_{11}$	70	230	13	[3]
$Ni_{46.4}Mn_{32.8}Sn_{20.8}$	5	239	12	[73]
$Ni_{47}Fe_3Mn_{36}Sn_{14}$	10	75	9	[74]
$Ni_{50}Mn_{34}In_{15.5}Al_{0.5}$	50	215	5	[75]

[1] S. Y. Yu, Z. H. Liu, G. D. Liu, J. L. Chen, Z. X. Cao, G. H. Wu, B. Zhang, and X. X. Zhang, Appl. Phys. Lett. **89**, 162503 (2006).

[2] K. Koyama, H. Okada, K. Watanabe, T. Kanomata, R. Kainuma, W. Ito, K. Oikawa, and K. Ishida, Appl. Phys. Lett. **89**, 182510 (2006).

[3] S. Y. Yu, L. Ma, G. D. Liu, Z. H. Liu, J. L. Chen, Z. X. Cao, and G. H. Wu, Appl. Phys. Lett. **90**, 242501 (2007).

[4] R. Kainuma, Y. Imano, W. Ito, Y. Sutou, H. Morito, S. Okamoto, O. Kitakami, K. Oikawa, A. Fujita, T. Kanomata, and K. Ishida, Nature (London) **439**, 957 (2006).

[5] R. Kainuma, Y. Imano, W. Ito, H. Morito, Y. Sutou, K. Oikawa, A. Fujita, K. Ishida, S. Okamoto, O. Kitakami, and T. Kanomata, Appl. Phys. Lett. **88**, 192513 (2006).

[6] T. Krenke, E. Duman, M. Acet, E. F. Wassermann, X. Moya, L. Mañosa, A. Planes, E. Suard, and B. Ouladdiaf, Phys. Rev. B **75**, 104414 (2007) .

[7] T. Krenke, E. Duman, M. Acet, E. F. Wassermann, X. Moya, L. Mañosa, and A. Planes, Nat. Mater. **4**, 450 (2005).

[8] M. Khan, N. Ali, and S. Stadler, J. Appl. Phys. **101**, 053919 (2007).

[9] J. Liu, T. Gottschall, K. P. Skokov, J. D. Moore, and O. Gutfleisch, Nat. Mater. **11**, 620 (2012).

[10] T. Gottschall, K. P. Skokov, B. Frincu, and O. Gutfleisch, Appl. Phys. Lett. **106**, 021901 (2015).

[11] B. Zhang, X. X. Zhang, S. Y. Yu, J. L. Chen, Z. X. Cao, and G. H. Wu, Appl. Phys. Lett. **91**, 012510 (2007).

[12] M. Takagishi, K. Koi, M. Yoshikawa, T. Funayama, H. Iwasaki, and M. Sahashi, IEEE Trans. Magn. **38**, 2277 (2002).

[13] K. Ullakko, J. K. Huang, C. Kantner, R. C. O'Handley, and V. V. Kokorin, Appl. Phys. Lett. **69**, 1966 (1996).

[14] J. Liu, T. G. Woodcock, N. Scheerbaum, and O. Gutfleisch, Acta Mater. **57**, 4911 (2009).

[15] Z. D. Han, D. H. Wang, C. L. Zhang, H. C. Xuan, J. R. Zhang, B. X. Gu, and Y. W. Du, J. Appl. Phys. **104**, 053906 (2008).

[16] L. Huang, D. Y. Cong, L. Ma, Z. H. Nie, M. G. Wang, Z. L. Wang, H. L. Suo, Y. Ren, and Y. D. Wang, J. Alloys Compd. **647**, 1081 (2015).

[17] V. K. Sharma, M. K. Chattopadhyay, K. H. B. Shaeb, A. Chouhan, and S. B. Roy, Appl. Phys. Lett. **89**, 222509 (2006).

[18] K. Ito, W. Ito, R. Y. Umetsu, S. Tajima, H. Kawaura, R. Kainuma, and K. Ishida, Scr. Mater. **61**, 504 (2009).

[19] H. E. Karaka, I. Karaman, B. Basaran, D. C. Lagoudas, Y. I. Chumlyakov, and H. J. Maier, Acta Mater. **55**, 4253 (2007).

[20] L. Huang, D. Y. Cong, L. Ma, Z. H. Nie, Z. L. Wang, H. L. Suo, Y. Ren, and Y. D. Wang, Appl. Phys. Lett. **108**, 032405 (2016).

[21] Y. H. Qu, D. Y. Cong, X. M. Sun, Z. H. Nie, W. Y. Gui, R. G. Li, Y. Ren, and Y. D. Wang, Acta Mater. **134**, 236 (2017).

[22] J. A. Monroe, I. Karaman, B. Basaran, W. Ito, R. Y. Umetsu, R. Kainuma, K. Koyama, and Y. I. Chumlyakov, Acta Mater. **60**, 6883 (2012).

[23] D. W. Zhao, J. Liu, X. Chen, W. Sun, Y. Li, M. X. Zhang, Y. Y. Shao, H. Zhang, and A. Yan, Acta Mater. **133**, 217 (2017).

[24] H. Hua, J. M. Wang, C. B. Jiang, and H. B. Xu, Scr. Mater. **124**, 142 (2016).

[25] J. Liu, S. Aksoy, N. Scheerbaum, M. Acet, and O. Gutfleisch, Appl. Phys. Lett. **95**, 232515 (2009).

[26] S. Y. Yu, A. J. Gu, S. S. Kang, S. J. Hu, Z. C. Li, S. T. Ye, H. H. Li, J. J. Sun, and R. R. Hao, J. Alloys Compd. **681**, 1 (2016).

[27] Y. H. Qu, D. Y. Cong, Z. Chen, W. Y. Gui, X. M. Sun, S. H. Li, L. Ma, and Y. D. Wang, Appl. Phys. Lett. **111**, 192412 (2017).

[28] W. Ito, Y. Imano, R. Kainuma, Y. Sutou, K. Oikawa, and K. Ishida, Metall. Mater. Trans. A **38**, 759 (2007).

[29] S. Kustov, M. L. Corró, J. Pons, and E. Cesari, Appl. Phys. Lett. **94**, 191901 (2009).

[30] V. Recarte, J. I. Pérez-Landazábal, V. Sánchez-Alarcos, V. Zablotskii, E. Cesari, and S. Kustov, Acta Mater. **60**, 3168 (2012).

[31] B. Emre, N. M. Bruno, S. Yuce Emre, and I. Karaman, Appl. Phys. Lett. **105**, 231910 (2014).

[32] T. Samanta, A. Us Saleheen, D. L. Lepkowski, A. Shankar, I. Dubenko, A. Quetz, M. Khan, N. Ali, and S. Stadler, Phys. Rev. B **90**, 064412 (2014).

[33] A. K. Nayak, K. G. Suresh, and A. K. Nigam, J. Phys. D: Appl. Phys. **42**, 035009 (2009).

[34] L. Huang, D. Y. Cong, H. L. Suo, and Y. D. Wang, Appl. Phys. Lett. **104**, 132407 (2014).

[35] V. Franco, J. S. Blázquez, J. J. Ipus, J. Y. Law, L. M. Moreno-Ramírez, and A. Conde, Prog. Mater. Sci. **93**, 112 (2018).

[36] D. Y. Cong, L. Huang, V. Hardy, D. Bourgault, X. M. Sun, Z. H. Nie, M. G. Wang, Y. Ren, P. Entel, and Y. D. Wang, Acta Mater. **146**, 142 (2018).

[37] T. Gottschall, K. P. Skokov, R. Burriel, and O. Gutfleisch, Acta Mater. **107**, 1 (2016).

[38] Z. Yang, D. Y. Cong, X. M. Sun, Z. H. Nie, and Y. D. Wang, Acta Mater. **127**, 33 (2017).

[39] H. C. Xuan, D. H. Wang, C. L. Zhang, Z. D. Han, B. X. Gu, and Y. W. Du, Appl. Phys. Lett. **92**, 102503 (2008).

[40] V. K. Sharma, M. K. Chattopadhyay, A. Khandelwal, and S. B. Roy, Phys. Rev. B **82**, 172411 (2010).

[41] E. Stern-Taulats, A. Planes, P. Lloveras, M. Barrio, J.-L. Tamarit, S. Pramanick, S. Majumdar, S. Yüce, B. Emre, C. Frontera, and L. Mañosa, Acta Mater. **96**, 324 (2015).

[42] V. A. Chernenko, Scr. Mater. **40**, 523 (1999).

[43] T. Krenke, M. Acet, E. F. Wassermann, X. Moya, L. Mañosa, and A. Planes, Phys. Rev. B **73**, 174413 (2006).

[44] L. Zhou, A. Mehta, A. Giri, K. Cho, and Y. Sohn, Mater. Sci. Eng. A **646**, 57 (2015).

[45] F. X. Hu, J. Wang, J. Shen, B. Gao, J. R. Sun, and B. G. Shen, J. Appl. Phys. **105**, 07A940 (2009).

[46] F. S. Liu, Q. B. Wang, W. Q. Ao, Y. J. Yu, L. C. Pan, and J. Q. Li, J. Magn. Magn. Mater. **324**, 514 (2012).

[47] A. J. Studer, M. E. Hagen, and T. J. Noakes, Phys. B: Condens. Matter **385-386**, 1013 (2006).

[48] X. Moya, L. Mañosa, A. Planes, S. Aksoy, M. Acet, E. F. Wassermann, and T. Krenke, Phys. Rev. B **75**, 184412 (2007).

[49] H. F. Tian, J. B. Lu, L. Ma, H. L. Shi, H. X. Yang, G. H. Wu, and J. Q. Li, J. Appl. Phys. **112**, 033904 (2012).

[50] Z. Y. Zhang, R. D. James, and S. Müller, Acta Mater. **57**, 4332 (2009).

[51] Y. Song, X. Chen, V. Dabade, T. W. Shield, and R. D. James, Nature (London) **502**, 85 (2013).

[52] R. Delville, S. Kasinathan, Z. Y. Zhang, J. V. Humbeeck, R. D. James, and D. Schryvers, Philos. Mag. A **90**, 177 (2010).

[53] K. F. Hane and T. W. Shield, Acta Mater. **47**, 2603 (1999).

[54] V. Srivastava, Y. Song, K. Bhatti, and R. D. James, Adv. Energy Mater. **1**, 97 (2011).

[55] X. M. Sun, D. Y. Cong, K.-D. Liss, Y. H. Qu, L. Ma, H. L. Suo, and Y. D. Wang, Appl. Phys. Lett. **110**, 132402 (2017).

[56] C. Chluba, W. W. Ge, R. L. de Miranda, J. Strobel, L. Kienle, E. Quandt, and M. Wuttig, Science **348**, 1004 (2015).
[57] E. Stern-Taulats, P. O. Castillo-Villa, L. Mañosa, C. Frontera, S. Pramanick, S. Majumdar, and A. Planes, J. Appl. Phys. **115**, 173907 (2014).
[58] D. Y. Cong, S. Roth, and L. Schultz, Acta Mater. **60**, 5335 (2012).
[59] M. G. Zavareh, C. S. Mejía, A. K. Nayak, Y. Skourski, J. Wosnitza, C. Felser, and M. Nicklas, Appl. Phys. Lett. **106**, 071904 (2015).
[60] J. Liu, N. Scheerbaum, J. Lyubina, and O. Gutfleisch, Appl. Phys. Lett. **93**, 102512 (2008).
[61] V. K. Pecharsky and K. A. Gschneidner Jr., J. Appl. Phys. **86**, 6315 (1999).
[62] G. J. Liu, J. R. Sun, J. Shen, B. Gao, H. W. Zhang, F. X. Hu, and B. G. Shen, Appl. Phys. Lett. **90**, 032507 (2007).
[63] B. Emre, S. Yüce, E. Stern-Taulats, A. Planes, S. Fabbrici, F. Albertini, and L. Mañosa, J. Appl. Phys. **113**, 213905 (2013).
[64] Y. H. Qu, D. Y. Cong, S. H. Li, W. Y. Gui, Z. H. Nie, M. H. Zhang, Y. Ren, and Y. D. Wang, Acta Mater. **151**, 41 (2018).
[65] V. Provenzano, A. J. Shapiro, and R. D. Shull, Nature (London) **429**, 853 (2004).
[66] M. K. Chattopadhyay, V. K. Sharma, and S. B. Roy, Appl. Phys. Lett. **92**, 022503 (2008).
[67] V. K. Sharma, M. K. Chattopadhyay, L. S. Chandra, and S. B. Roy, J. Phys. D: Appl. Phys. **44**, 145002 (2011).
[68] K. Ullakko, Y. Ezer, A. Sozinov, G. Kimmel, P. Yakovenko, and V. K. Lindroos, Scr. Mater. **44**, 475 (2001).
[69] A. Fujita, K. Fukamichi, F. Gejima, R. Kainuma, and K. Ishida, Appl. Phys. Lett. **77**, 3054 (2000).
[70] C. Jing, X. L. Wang, P. Liao, Z. Li, Y. J. Yang, B. J. Kang, D. M. Deng, S. X. Cao, J. C. Zhang, and J. Zhu, J. Appl. Phys. **114**, 063907 (2013).
[71] Z. Li, K. Xu, Y. L. Zhang, and C. Jing, J. Appl. Phys. **117**, 023902 (2015).
[72] Y. Q. Zhang, Z. D. Zhang, and J. Aarts, Phys. Rev. B **70**, 132407 (2004).
[73] P. Lázpita, V. A. Chernenko, J. M. Barandiarán, I. Orue, J. Gutiérrez, J. Feuchtwanger, and J. A. Rodriguez-Velamazán, Mater. Sci. Forum **635**, 89 (2010).
[74] P. Liao, C. Jing, D. Zheng, Z. Li, B. J. Kang, D. M. Deng, S. X. Cao, B. Lu, and J. C. Zhang, Solid State Commun. **217**, 28 (2015).
[75] Y. Q. Wu, S. P. Guo, S. Y. Yu, H. Cheng, R. L. Wang, H. B. Xiao, L. F. Xu, R. Xiong, Y. Liu, Z. C. Xia, and C. P. Yang, Sci. Rep. **6**, 26068 (2016).